GRAPHICAL MODELS AND IMAGE PROCESSING
Vol. 59, No. 6, November, pp. 434–445, 1997
ARTICLE NO. IP970439

Nonparametric Estimation and Simulation of Two-Dimensional Gaussian Image Textures

Thomas C. M. Lee

Department of Statistics, Macquarie University and CSIRO Mathematical and Information Sciences, North Ryde, New South Wales 2113, Australia

and

Mark Berman

CSIRO Mathematical and Information Sciences, North Ryde, New South Wales 2113, Australia

Received July 1, 1996; revised June 12, 1997; accepted July 3, 1997

The work to be described is motivated by the need to simulate a variety of real–world image textures, all of which can be well approximated by stationary Gaussian random fields (SGRFs). Specifically, given an observed SGRF T, we wish to simulate SGRFs which look like and possess similar statistical properties to T. The main contribution of this paper is the development of an automatic and nonparametric spectrum estimation procedure which is able to produce an estimated spectrum of T in such a way that SGRFs simulated from this estimated spectrum have these desirable characteristics. Two special features of the procedure are: (i) it relies on a different risk function to that commonly used in nonparametric spectrum estimation, and (ii) it chooses its smoothing parameters by the technique of unbiased risk estimation. Results from a simulation study and a practical example demonstrate the good performance of the procedure. The practical example also illustrates how the proposed procedure can be combined with Monte Carlo testing to tackle target testing problems. Finally, the procedure is applied to the synthesis of some Brodatz textures, with some success.

1. INTRODUCTION

The work described below is motivated by the need to simulate a variety of real-world textured images, in order to answer a variety of questions about them. (An abridged conference version can be found in [21].) As an example, consider the two images taken from boreholes, shown in Fig. 1. For these images, the objective is to test for the existence of any crack–like features: there are two obvious cracks, from top to bottom in Fig. 1(a) while there are no apparent cracks in Fig. 1(b). Note also the quite different background textures in the two images. More generally, we are interested in developing an automatic method for testing the existence of features occupying a relatively small number of pixels on a textured background. For most real-world images, the probability theory underlying such a testing procedure appears to be intractable. One solution to this is to use *Monte Carlo testing* (for example see [31] and [9]). The general idea is: given an observed image T, first simulate m different image textures which are similar to the background texture of T (i.e., under the null hypothesis of no cracks present), and then compare T with these m simulated textures using an appropriate summary statistic for each image to see if there is a significant difference. Section 5 provides an illustrative example.

In this paper image textures that can be well modeled by stationary Gaussian random fields (SGRFs) will receive primary attention (e.g., [6]). Our objective is to propose an automatic and nonparametric spectrum estimator which is designed to produce an estimated spectrum of an observed SGRF in such a way that any subsequent SGRFs simulated from this estimated spectrum would (i) look like and (ii) possess similar statistical properties to the observed SGRF. This contrasts with the traditional approach to spectral estimation, which does not consider the issue of simulating SGRFs from the estimated spectrum. In the process of constructing such a spectral estimator, we have discovered that the choice of the risk function for evaluating the quality of fit is of primary importance, and we believe this is a major finding of the paper. We will illustrate our point in later sections.

Other methods for spectral estimation of SGRFs have also been proposed in the literature; see [20; 3, Addendum; 10, Chap. 6; 15, Chap. 6] for some general discussions. These methods include autoregressive moving-average (ARMA) modeling (e.g., [17, 18, 35]) and maximum entropy techniques (e.g., [19, 34]). In addition, Solo [37] has proposed a class of parametric models based on the cep-

1077-3169/97 $25.00

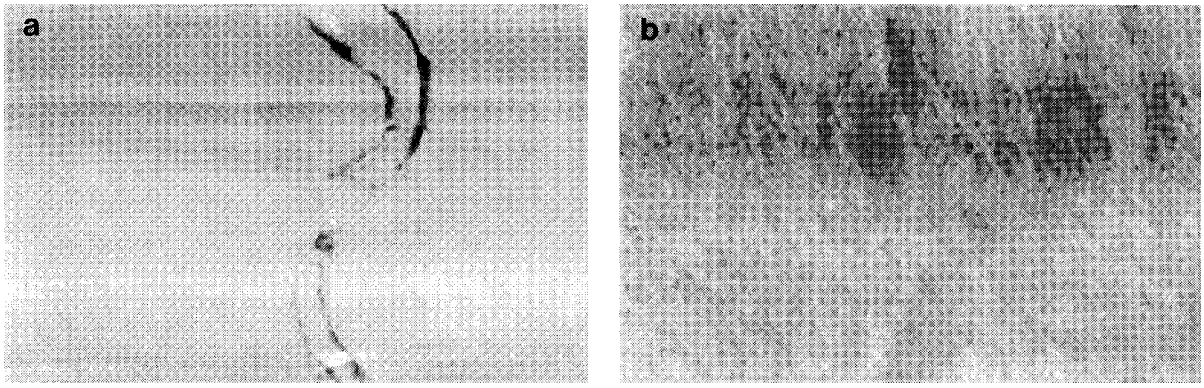

FIG. 1. Two images taken from boreholes. Size of each image: 280 × 432 pixels.

strum (Fourier series of the spectrum). He also discusses some shortcomings of the ARMA approach.

Among other popular random field models such as Markov random fields (for example, see the pioneering papers [13] and [2]), one attractive property of SGRFs is that fast and exact estimation and simulation methods exist. The spectrum estimator to be described below can be rapidly computed via the Fourier domain. For fast methods of simulating SGRFs from a given spectrum, see [42] and references given therein. In addition, Appendix B gives details of the Fourier based method we have used for simulating SGRFs.

The rest of this article is organized as follows. Section 2 provides some background and discusses several risk functions. Section 3 describes the proposed spectrum estimator and provides a comparison of some nonparametric spectrum estimators. Section 4 reports the results of a simulation study. In Section 5 the borehole images are revisited and in Section 6 we investigate the applicability of SGRFs for general texture modelling. Mathematical details are given in Appendix A.

2. BACKGROUND AND RISK FUNCTIONS

Let $S = \{x_{st}, s, t = 0, \pm 1, \pm 2, \ldots\}$ be a two dimensional equally-spaced and real-valued stationary process with autocovariance function

$$\gamma_{kl} = E(x_{st}x_{s+k,t+l}), \quad k, l = 0, \pm 1, \pm 2, \ldots$$

and spectrum

$$f(\omega_1, \omega_2) = \frac{1}{4\pi^2} \sum_{k,l} \gamma_{kl} \exp(-i(k\omega_1 + l\omega_2)),$$
$$\omega_1, \omega_2 \in [0, 2\pi).$$

Suppose we observed a rectangular subset T of $S: T = \{x_{st}, (s, t) \in A\}$, where $A = \{(s, t) : 0 \le s < n_1, 0 \le t < n_2\}$ is a set of indices. This set T is an observed image of size n_1 by n_2. The periodogram I is defined as:

$$I(\omega_1, \omega_2) = \frac{1}{4\pi^2 n_1 n_2} \left| \sum_{s,t} \gamma_{kl} \exp(-i(s\omega_1 + t\omega_2)) \right|^2,$$
$$\omega_1, \omega_2 \in [0, 2\pi).$$

To simplify notation, define f_{st} as $f(2\pi s/n_1, 2\pi t/n_2)$ for $(s, t) \in A$, and similarly for I_{st}. According to Section IX of the Addendum of [3] (see also [31, Chap. 5]), under some mild regularity conditions, if both n_1 and n_2 are large, the approximation

$$I_{st} \approx f_{st}\varepsilon_{st}, \quad (s, t) \in A \tag{1}$$

holds, where all ε_{st}'s are independent random variables distributed as the standard exponential distribution, with the exception that ε_{00}, $\varepsilon_{n_1/2,0}$ (if n_1 is even), $\varepsilon_{0,n_2/2}$ (if n_2 is even), and $\varepsilon_{n_1/2,n_2/2}$ (if both n_1 and n_2 are even) are χ^2_1 random variables. If n_1 and/or n_2 are small, tapering can be applied in order to reduce the bias of the periodogram, and (1) remains approximately valid (see [8]). From now on ε_{00}, $\varepsilon_{n_1/2,0}$ $\varepsilon_{0,n_2/2}$, and $\varepsilon_{n_1/2,n_2/2}$ will be treated as if they were standard exponentially distributed, and the approximation (1) is assumed to be exact. As can be seen below, the effect of these changes is asymptotically negligible. In order to guard against extreme observations of I_{00}, $I_{n_1/2,0}$ $I_{0,n_2/2}$, and $I_{n_1/2,n_2/2}$ one can simply replace them with values obtained by interpolating their neighboring observations. Hence we have the following model:

$$\begin{cases} I_{st} = f_{st}\varepsilon_{st}, \quad (s, t) \in A, \\ \varepsilon_{st} : \text{independent standard exponential} \\ \quad \text{random variables.} \end{cases} \tag{2}$$

If the spectrum f is strictly positive, the *multiplicative* model (2) can be transformed to an *additive* model by taking a logarithmic transform

$$\begin{cases} \log I_{st} + \psi(1) = \log f_{st} + \xi_{st}, \quad (s,t) \in A, \\ \xi_{st} : \text{independent zero mean random variables} \\ \quad \text{with variance } \pi^2/6, \end{cases} \tag{3}$$

where $\psi(x)$ is the digamma function (the derivative of the gamma function) with $\psi(1) = 0.57722$. Therefore, the spectrum f can be estimated nonparametrically either by: (i) smoothing the periodogram under the condition that the errors (ε_{st}) are multiplicative or (ii) after adjusting for the constant $\psi(1)$, smoothing the log-periodogram ($\log I_{st}$), followed by an antilogarithmic transform. In the latter case the errors (ξ_{st}) are additive and hence standard nonparametric curve estimation techniques can be applied.

For evaluating the quality of a particular set of estimates $\hat{f}_{st}$ for f_{st}, the three most commonly used risk functions are:

$$\text{Risk}_1 = \frac{1}{n_1 n_2} E\left[\sum_{s,t} (f_{st} - \hat{f}_{st})^2\right],$$

$$\text{Risk}_2 = \frac{1}{n_1 n_2} E\left[\sum_{s,t} (\log(f_{st}) - \log(\hat{f}_{st}))^2\right],$$

$$\text{Risk}_3 = \frac{1}{n_1 n_2} E\left[\sum_{s,t} ((f_{st} - \hat{f}_{st})/f_{st})^2\right],$$

with Risk_2 receiving primary attention in the literature. Notice that Risk_2 and Risk_3 are locally equivalent as $\log(1 + x) \approx x$ for small x. However, for the current purpose (i.e., any SGRFs simulated from the estimates $\hat{f}_{st}$'s should look like and possess roughly the same statistical properties of the observed image), it is argued that one should use the risk function Risk_1 rather than Risk_2 or Risk_3. The reasons are:

1. Many image textures (and certainly those that can be modeled as SGRFs) are relatively continuous and devoid of edges. Consequently, in such image textures, most of the power is concentrated in the low frequency region of the spectrum. However, the risk functions Risk_2 and Risk_3 implicitly allocate more weight to frequencies with small magnitudes than does Risk_1, and typically in Gaussian image textures these small magnitude frequencies are concentrated in the high frequency region of the spectrum (this situation is accentuated in 2D data because the proportion of high frequencies there is much higher than in 1D data). Consequently, Risk_2 and Risk_3 primarily measure the quality of fit of the high frequencies in Gaussian image textures, while Risk_1 primarily measures the quality of fit in the more relevant low frequencies. Simulation results to be reported in Section 4 support this argument.

2. The use of Risk_2 or Risk_3 implies the assumption that the spectrum is strictly positive (i.e., no zero values are allowed). This assumption is often violated (or nearly so) by Gaussian image textures and can cause numerical problems when taking logarithms or reciprocals.

3. SOME PROCEDURES FOR NONPARAMETRIC SPECTRUM ESTIMATION

If Risk_1 is used as the risk function, it is natural (although not necessary) to smooth the periodogram rather than its logarithm. In Section 3.1 a nonparametric spectrum estimator which directly smoothes the periodogram is proposed. A brief discussion of some nonparametric spectrum estimators which aim to minimize Risk_2 (all of which smooth the log-periodogram) is given in Section 3.2.

3.1. *A Proposed Procedure Based on Periodogram Smoothing*

Two special features of the proposed procedure are: (i) it works under model (2) which assumes multiplicative errors (in contrast to other standard nonparametric curve estimation methods which assume additive errors) and (ii) the smoothing parameters involved are automatically chosen by unbiased risk estimation—a technique similar to Mallows' C_p [22].

The procedure estimates a spectrum by applying weighted local smoothing to its corresponding periodogram. The estimator is defined as

$$\hat{f}_{st} = \sum_{i=-p}^{p} \sum_{j=-q}^{q} w_{ij} I_{s+i,t+j}, \quad (s,t) \in A, \tag{4}$$

where $2p + 1$ and $2q + 1$ are the spans for smoothing in the s- and t-directions, respectively, and w_{ij}, $i = -p, \ldots, p$, $j = -q, \ldots, q$ are nonnegative weights satisfying

$$w_{|i|,|j|} = w_{ij} \quad \text{and} \quad \sum_{i,j} w_{ij} = 1.$$

The weight at the center w_{00} should also be a decreasing function of p and q. These conditions are satisfied by almost all suitably discretized kernel functions commonly used for multivariate kernel smoothing (e.g., see [41, Chap. 4]). In this paper we shall use the weights

$$w_{ij} = w'_{ij} \left(\sum_{u,v} w'_{uv}\right)^{-1}, \quad w'_{uv} = \frac{2}{\pi pq}\left(1 - \frac{u^2}{p^2} - \frac{v^2}{q^2}\right)_+, \tag{5}$$

for $i, u = -p, \ldots, p$ and $j, v = -q, \ldots, q$, and $(x)_+$ means $\max(x, 0)$. These weights can be seen as a discrete version

of the optimal weight function derived in [11]. One can certainly use other weights but the gain (if any) is expected to be minimal, as it is widely known that the choice of the kernel/weight function in the nonparametric kernel smoothing context is not an important issue. For example see [36, Chaps. 3 and 4] and [41, Chap. 4].

The weights w_{ij}'s certainly depend on p and q. However for the sake of clarity, this dependence is suppressed in the notation of w_{ij}'s. Since the spectrum is periodic with period 2π, boundary points in (4) are handled by periodic smoothing.

For the estimator defined in (4), there are two smoothing parameters (p and q) independently controlling the amount of smoothing in each coordinate direction. In fact, as discussed in [40], up to three independent smoothing parameters can be incorporated for the smoothing of a two-dimensional surface: two for direction and one for orientation. This paper also concluded that a kernel-type estimator should have the ability to smooth independently by different amounts in each direction (such as (4)), and it is quite often that this will provide satisfactory performance.

Now we address the issue of how to choose (p, q). As discussed in Section 2, (p, q) should be chosen to minimize the risk function Risk_1, henceforth written as $\text{Risk}_1(p, q)$ to indicate that it is a function of (p, q). Since $\text{Risk}_1(p, q)$ is unknown, a standard approach is to form an unbiased estimator of $\text{Risk}_1(p, q)$ and choose (p, q) to minimize this risk estimator. For the smoothing of one-dimensional periodograms, [14] mentioned the use of cross-validation (apparently it is presented in the technical report [27], which we are unable to obtain), and it can be generalized to the present setting: (p, q) is chosen to be the minimizer of the cross-validation score

$$\text{CV}(p, q) = \frac{\text{RSS}}{n_1 n_2 (1 - w_{00})^2},$$

where $\text{RSS} = \Sigma(I_{st} - \hat{f}_{st})^2$ is the residual sum of squares. However, it is straightforward to show that $\text{CV}(p, q)$ is biased when n_1 and/or n_2 are finite. It is known that for low-dimensional parameter estimation problems, biased estimators could potentially lead to serious estimation errors. Therefore even though there is no rigorous analysis showing that the use of $\text{CV}(p, q)$ as an estimator for $\text{Risk}_1(p, q)$ would suffer from similar problems, intuitively it is preferable to use an unbiased estimator for $\text{Risk}_1(p, q)$. By using a technique similar to Mallows' C_p, we are able to develop an unbiased estimator for $\text{Risk}_1(p, q)$ (under model (2)). It is shown in Appendix A that

$$\hat{\text{Risk}}_1(p, q) = \frac{\text{RSS}}{n_1 n_2} - \frac{(1 - 2w_{00})}{2n_1 n_2} \sum_{s,t} I_{st}^2 \qquad (6)$$

is an unbiased estimator of $\text{Risk}_1(p, q)$, and it is proposed to choose the minimizer $(p, q)_{\text{UR}}$ of $\hat{\text{Risk}}_1(p, q)$ as the spans.

We close this section with the following remark about the practical implementation of the procedure. Since estimator (4) is a convolution operation, when n_1 and n_2 are large (which is typical for image data), a substantial saving of computation time can be made if the estimates $\hat{f}_{st}$'s are computed via the Fourier domain, especially when p and q are large (e.g., see [33, Chap. 2]). The use of the Fourier method in this situation would not introduce any boundary problems, as the spectrum is periodic. Also, by Parseval's theorem, the residual sum of squares (RSS) can be expressed in terms of the Fourier transforms of $\hat{f}_{st}$'s and I_{st}'s. This means when one is searching for p and q to minimize $\text{Risk}_1(p, q)$, there is no need to invert the Fourier transform to obtain each $\hat{f}_{st}$.

3.2. *Some Smoothing Procedures Based on the Log-Periodogram*

An analogous procedure similar to the one described above can be developed for log-periodogram smoothing. This procedure naturally uses Risk_2 as the risk function to measure the quality of fit. Assume the spectrum is strictly positive and define $y_{st} = \log I_{st} + 0.57722$. Then under the additive model (3), $E(y_{st}) = \log f_{st}$, and thus f_{st} can be estimated by

$$\tilde{f}_{st} = \exp(\tilde{g}_{st}), \quad \tilde{g}_{st} = \sum_{i=-p'}^{p'} \sum_{j=-q'}^{q'} w_{ij} y_{s+i,t+j}, \quad (s, t) \in A, \quad (7)$$

with the spans (p', q') chosen as the minimizer $(p', q')_{\text{UR}}$ of

$$\hat{\text{Risk}}_2(p', q') = \frac{\Sigma(y_{st} - \tilde{g}_{st})^2}{n_1 n_2} - \frac{(1 - 2w_{00})\pi^2}{6n_1 n_2}.$$

Using the same technique as in Appendix A, one can show that $\hat{\text{Risk}}_2$ is an unbiased estimator of Risk_2 (under model (3)). As for those $\hat{f}_{st}$'s, fast computation of $\tilde{g}_{st}$'s is made possible by Fourier methods.

Since the errors are additive, other fast spatial smoothers (which assume additive errors) can be applied to smooth the y_{st}'s (and the natural risk function to be minimized is Risk_2). Berman [1] and Buckley [5] demonstrated that fast computations of the thin-plate smoothing spline can be performed for image data via the discrete Fourier transform and the discrete cosine transform, respectively. O'Sullivan [25] showed fast Laplacian smoothing can be achieved by using Fourier methods. As all the discussed smoothers can be computed via Fourier methods, it is expected that their computation times are of the same order.

In order to study the relative performances of a kernel type smoother and a spline type smoother, and between the

unbiased risk estimation choice and the cross-validation choice of spans, we applied three smoothers to some common log-periodograms. These smoothers are estimator $\tilde{g}_{st}$ in (7) with unbiased risk estimation choice of spans, estimator $\tilde{g}_{st}$ in (7) with cross-validation choice of spans, and Berman's spline smoother. Berman's spline smoother uses generalized cross-validation to choose its smoothing parameter, which is equivalent to cross-validation for regularly-spaced data. Provided that the amounts of smoothing chosen by these three smoothers did not differ by too much, the resulting smoothed periodograms gave similar mean squared errors, and in fact for most cases, the amounts of smoothing were well chosen (and similar) by these smoothers. We believe that the lessons that can be learned from this are that for the *practical* smoothing of image data: (i) there is no significant difference between using a kernel type or a spline type smoother and (ii) there is no significant difference between using an unbiased risk estimation (if the noise variance is known or can be well estimated) or a cross-validation based approach for automatic smoothing parameter selection. This is probably because for most image data, the total number of pixels is large enough for these two types of "residual-based" approaches to perform well.

4. SIMULATION RESULTS

The aim of this section is to demonstrate that the risk function Risk_1 is preferable to Risk_2 (which is locally equivalent to Risk_3) by means of a simulation study. Figure 2 displays a typical SGRF, observed in the square $[-1, 1) \times [-1, 1)$ with a 256×256 discretization, generated from the autocovariance function

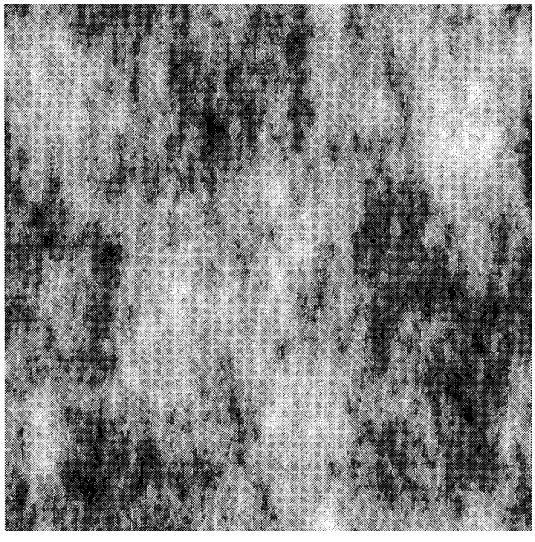

FIG. 2. A typical SGRF generated by autocovariance function (8).

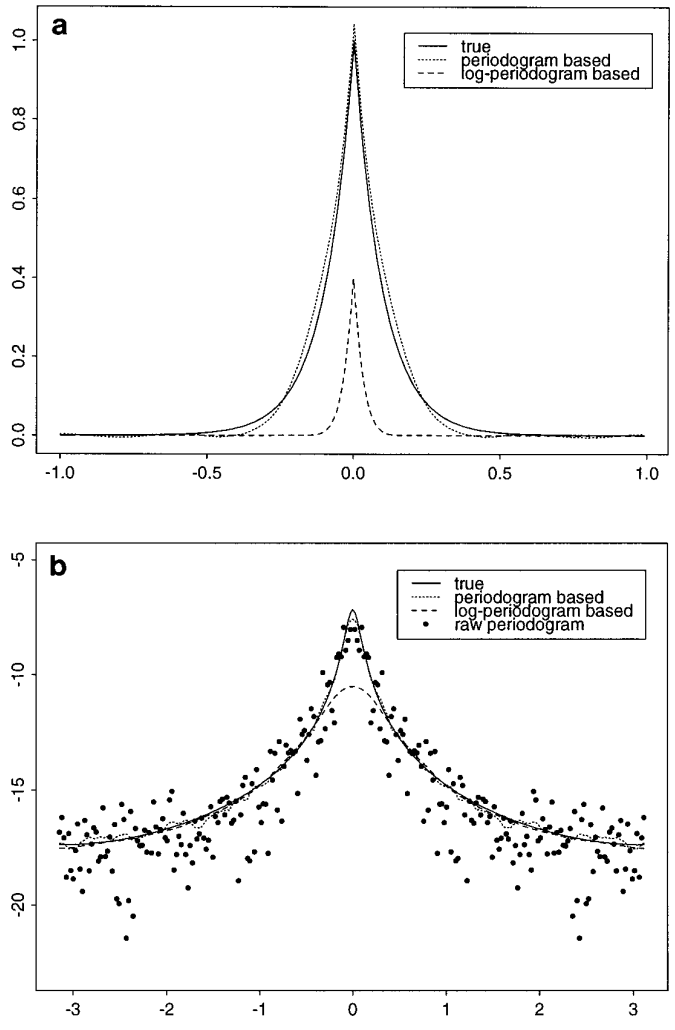

FIG. 3. Plots of various (a) autocovariance functions and (b) spectra. All spectra are plotted on the log scale.

$$\gamma_{kl} = \exp\left(-10\sqrt{\left(\frac{k}{128}\right)^2 + 4\left(\frac{l}{128}\right)^2}\right), \qquad (8)$$

for $k, l = 0, \pm 1, \pm 2, \ldots$. (Details of the simulation procedure we used are given in Appendix B.) Notice that (8) is not isotropic. For the range $k = 0, l = -128, \ldots, 127$, (8) is plotted in Fig. 3(a), and the corresponding portion of its spectrum is plotted in Fig. 3(b).

(All images in this paper are displayed after the following transform is applied. First the mean μ and the standard deviation σ of the gray values of an image are calculated. Then those gray values below $\mu - 3.5\sigma$ and above $\mu + 3.5\sigma$ are set to $\mu - 3.5\sigma$ and $\mu + 3.5\sigma$, respectively. Finally all gray values are linearly stretched so that the minimum and maximum values are 0 (black) and 255 (white), respectively.)

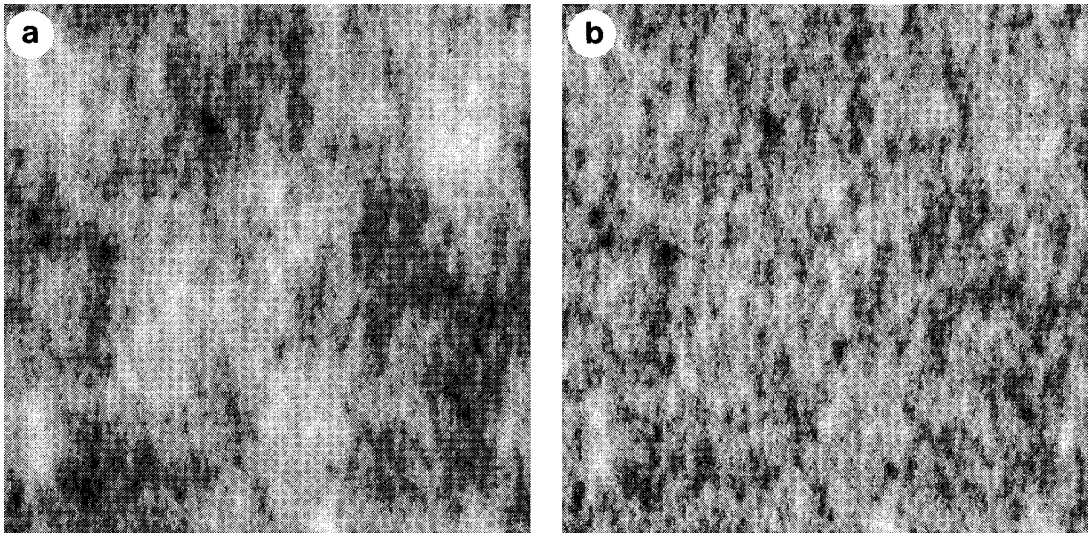

FIG. 4. Simulated SGRFs: (a) by the periodogram based procedure and (b) by the log–periodogram based procedure.

Here the SGRF displayed in Fig. 2 is the observed field. The periodogram based smoothing procedure (4) with unbiased risk estimation choice of spans $(p, q)_{\mathrm{UR}}$ and the log-periodogram based smoothing procedure (7) with unbiased risk estimation choice of spans $(p', q')_{\mathrm{UR}}$ were applied to estimate the spectrum with common weights w_{ij}'s given by (5).

The estimated spectra together with their corresponding estimated autocovariance functions (inverse Fourier transforms of the estimated spectra) are also plotted in Fig. 3. From Fig. 3(b) we can see that the log-periodogram based procedure produces a spectrum which is oversmoothed in the low frequency region. This is because Risk_2 (the risk function which this log-periodogram based procedure aims to minimize) substantially allocates more weight to the flat and smooth high frequency region of the spectrum, and this has caused the log-periodogram based procedure heavily to smooth the log-periodogram in order to produce smooth estimates of the high frequencies. Consequently, the low frequency region has been severely oversmoothed. We have observed the same phenomenon using other smoothers whenever Risk_2 is the risk function being minimized. This oversmoothing in the low frequency region drastically affects the quality of the estimated autocovariance function; see Fig. 3(a).

With the two estimated spectra, we simulated two SGRFs with the same random number generator seed that was used to simulate the original observed SGRF displayed in Fig. 2. That means, if a spectrum is perfectly estimated, the simulated SGRF would be identical to the observed one. The two simulated SGRFs are displayed in Fig. 4. By visual judgment it can be concluded that the periodogram based procedure is superior to the log-periodogram based procedure (and other Risk_2 type smoothers). We also plotted the gray value densities of the observed and the two simulated SGRFs in Fig. 5. Again, this shows that the periodogram based procedure is a better procedure.

We have also performed the same experiment on other 256×256 images with the autocovariance functions:

$$\gamma_{kl} = \exp(-200r^2),$$
$$\gamma_{kl} = \cos(10\pi r)/\exp(5\pi r),$$
$$\gamma_{kl} = \cos(10\pi r)/\exp(2\pi^2 r^2),$$

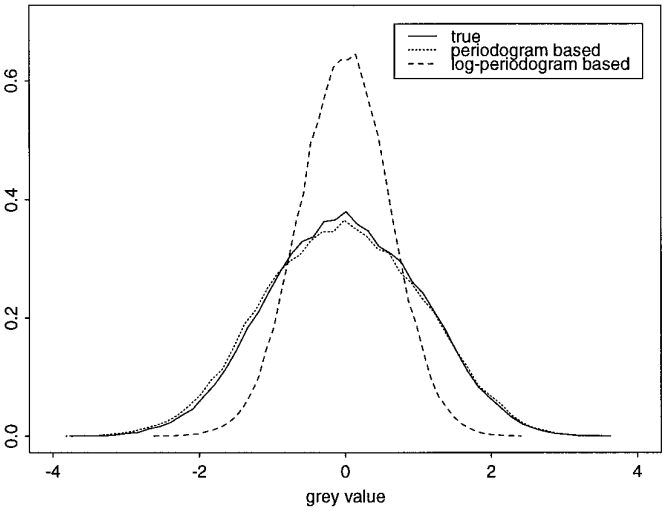

FIG. 5. Densities of various SGRFs.

where

$$r = \sqrt{\left(\frac{k}{128}\right)^2 + \left(\frac{l}{128}\right)^2}.$$

In each case, we obtained analogous results.

One of the referees of this paper suggested that Risk_1 may appear to be preferable to Risk_2 because we are working with gamma corrected images. To test this hypothesis, we compared the Risk_1 and Risk_2 based techniques on some images which were not gamma corrected. Our empirical results for these images still support the use of Risk_1.

5. AN APPLICATION TO HYPOTHESIS TESTING

As mentioned in Section 1, one of the motivations for our work is the need for a method for the automatic testing of the presence of cracks (or other features) in images, such as those displayed in Fig. 1. We adopted the following strategy: first find the vertical darkest path (defined below) in a borehole image and then test if this darkest path is ''dark enough'' to be classified as a crack. Since images might have been captured under unstable lighting conditions (therefore they are not stationary and may have different gray value distributions, as demonstrated in Fig. 1), it is often that an illumination correction transform is first applied to the images to make them stationary before any further processing is carried out. If necessary, the stationary image should also be transformed pixelwise to ensure that the image histogram is approximately Gaussian.

A simple but effective formula for transforming an image $\alpha = (\alpha_1, \ldots, \alpha_n)$ to a stationary image $\beta = (\beta_1, \ldots, \beta_n)$ is

$$\beta_i = \frac{20(\alpha_i - \text{smed}(\alpha_i))}{\text{lsd}(\alpha_i)} + 128, \tag{9}$$

where $\text{smed}(\alpha_i)$ is the *separable median* (defined below) of gray values in the rectangle of size s_1 rows by s_2 columns centered at pixel i, and $\text{lsd}(\alpha_i)$ is a robust estimate of the *local standard deviation* of the same rectangle:

$$\text{lsd}(\alpha_i) = \text{smed}(|\alpha_i - \text{med}(\alpha_i)|).$$

The separable median in a rectangle is defined as the median of all the row medians in that rectangle. Narendra [24] showed that the separable median filter can be computed faster and preserves corners better than the traditional two-dimensional median filter. Formula (9) usually returns β_i's that are within the range [0, 255].

Here we give the definition of a *vertical darkest path* (a *horizontal darkest path* can be similarly defined). A *vertical path* is a set of pixels, one per row, with the property that pixels of this set in adjacent rows are 8-connected neighbors. The *brightness* of a path is the sum of the gray values of the corresponding pixels in the image. That is, the smaller the sum, the darker (on average) the path is. The *darkest path* is defined as the path with the least brightness (if there is more than one path having the same least brightness, randomly select one as the darkest path). A fast and reliable method that uses a dynamic programming algorithm to find the darkest path in an image is described in [32].

We applied the stationarity transform (9) to the two borehole images (with $s_1 = 13$ and $s_2 = 21$) displayed in Fig. 1. We also applied the method described in [32] to find the darkest paths of the two transformed images. These two images with their darkest paths overlaid are displayed in Fig. 6.

Now the only remaining problem is to construct a procedure for testing whether a detected darkest path of an image is in fact a crack or not. Perhaps the simplest test is by the method of thresholding: compare the darkest path's brightness with a prechosen threshold. If the brightness is less than the threshold, then this darkest path is classified as a crack. However, these sorts of thresholding techniques are not robust to changes in texture, and a more reliable testing procedure can be constructed using Monte Carlo testing.

Suppose T is the stationarity transformed image we would like to test. The first step of the procedure is to use the spectrum estimator developed in Section 3.1 to estimate the spectrum of T as if there are no cracks in T. Since it is quite often the case that the number of ''nonbackground pixels'' in an image with a small number of cracks is only a small fraction of all the pixels in the image, it is reasonable to expect these ''nonbackground pixels'' would not substantially worsen the estimation result. Then with the estimated spectrum, simulate m different image backgrounds, and for each of these simulated backgrounds, calculate the brightness of its darkest path. These m different simulated backgrounds should resemble the background of T. Figure 7 displays two typical simulated image backgrounds for the two stationarity transformed borehole images (without their darkest paths) displayed in Fig. 6. Therefore there will be m different simulated darkest path brightnesses, and the final step is to compare the brightness of the darkest path of T with these m simulated brightnesses. If the darkest path's brightness in T is among the smallest of all simulated brightnesses, then there is strong evidence that the darkest path of T is in fact a crack.

We applied the above testing procedure to the two stationarity transformed borehole images with $m = 99$. The brightness of the darkest path of the image in Fig. 6(a) is in fact smaller than all its simulated brightnesses, and hence one can conclude with confidence that the image in Fig. 6(a) contains at least one crack. For the image in Fig. 6(b), the darkest path's brightness is larger than 48 of

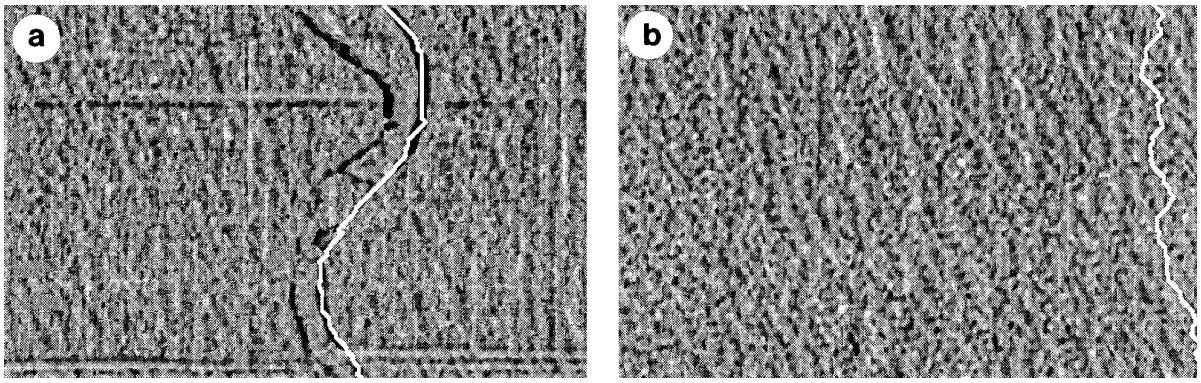

FIG. 6. Stationarity transformed borehole images with darkest paths (in white) overlaid.

its simulated brightnesses. Hence one can conclude with confidence that there are no cracks in the image displayed in Fig. 6(b).

6. WHEN ARE SGRFs APPROPRIATE FOR TEXTURE MODELING?

The technique developed in this paper strongly relies on the assumption that the target textures can be well modeled by SGRFs. In this section we briefly investigate the applicability of this assumption by applying the technique to synthesize some Brodatz textures [4].

Brodatz textures are widely used in the image processing literature as standard texture examples. For example see [6], [16], [26], [29], [39], and references given therein. We applied our technique to estimate the spectra of some Brodatz textures, and from these estimated spectra we synthesized some textures. The results are displayed in Figs. 8 and 9.

For textures 1 and 2, our technique performed reasonably well. However, for textures 3 and 4, our technique gave poor results. This is probably because SGRFs are very poor at capturing discontinuous structures. Paget and Longstaff [26] have developed an analogous procedure for texture synthesis using nonparametrically estimated Markov random fields. These authors applied their procedure to textures 3 and 4 and obtained successful results. However the time required for their approach to synthesize one texture image (or more precisely, to simulate one Markov random field) is enormous: for a 128×128 image, it takes 3 to 4 h on a parallel machine, while for our approach, it takes less than 1 s user time on a Sparc-10 workstation to synthesize a same-sized image (i.e., a SGRF) using the method briefly outlined in Appendix B.

7. DISCUSSION AND CONCLUSION

In this article we have demonstrated that, in the context of stationary Gaussian texture simulation, the choice of risk function for evaluating estimate quality is important: Risk_1 should be taken as the risk function. We have proposed an automatic and nonparametric spectrum estimation procedure which aims to minimize Risk_1. In addition, we illustrated via an example how the proposed technique can be combined with Monte Carlo testing to tackle target testing problems.

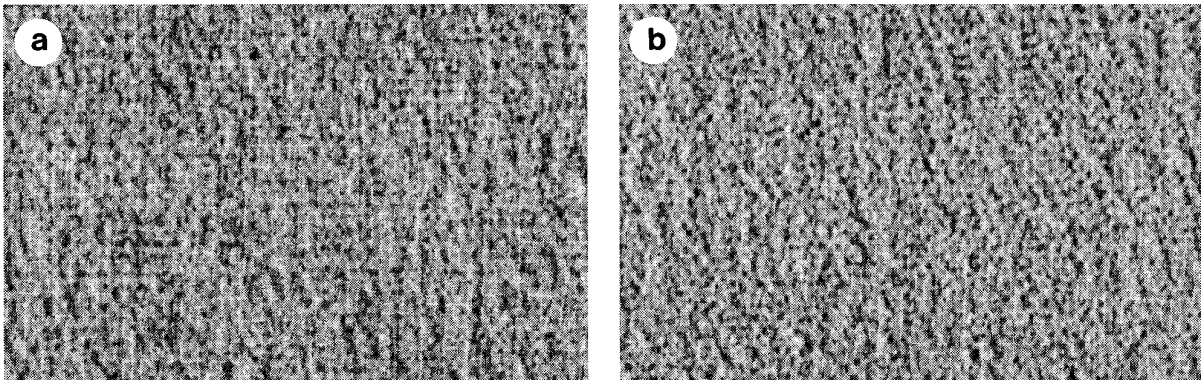

FIG. 7. Two typical simulated image backgrounds for images in Fig. 6(a) and Fig. 6(b).

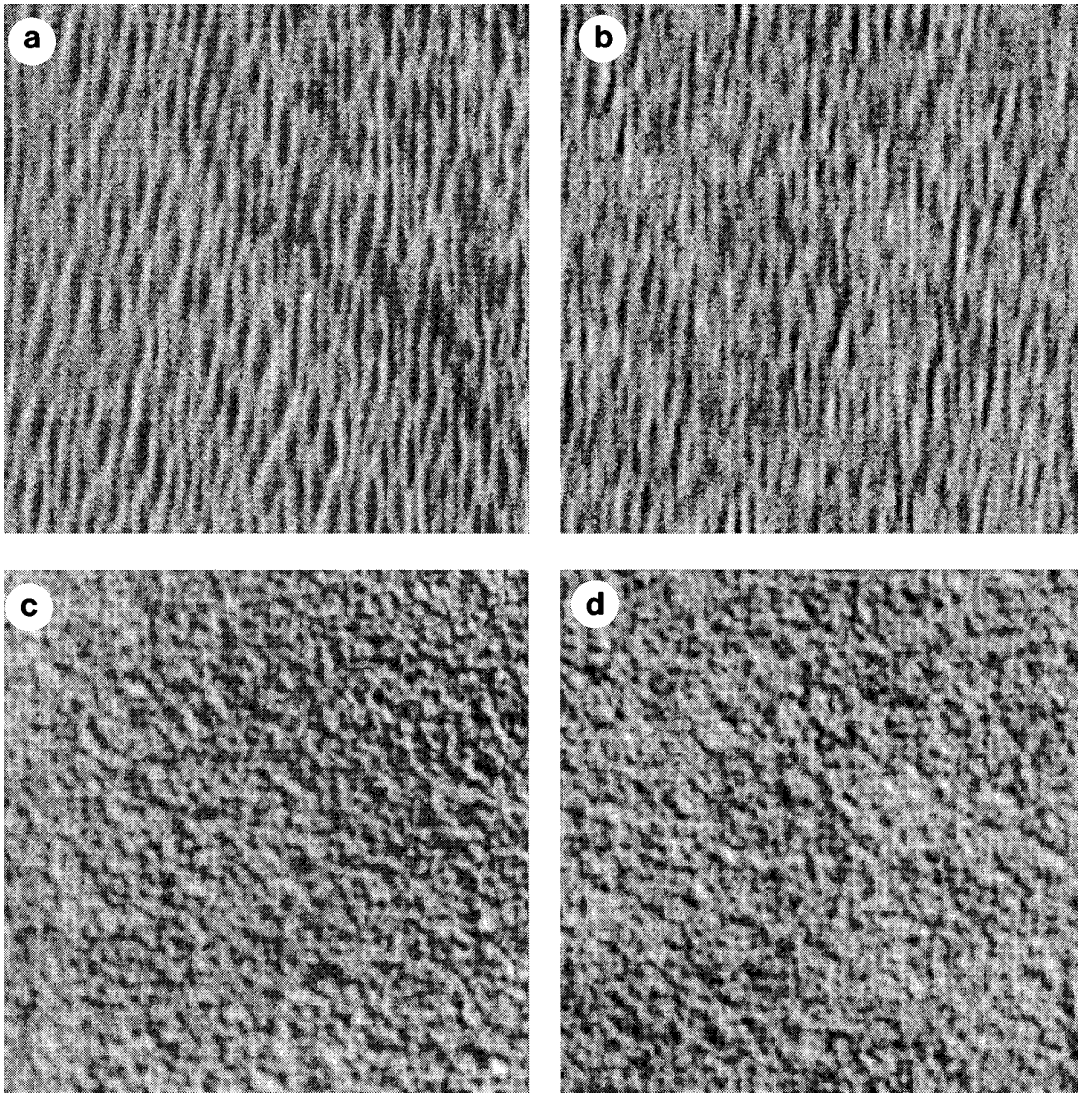

FIG. 8. Comparison of real and synthesized Brodatz's textures: results satisfactory. (a) real texture 1, (b) synthesized texture 1, (c) real texture 2, and (d) synthesized texture 2.

In this example, our estimate of the spectrum is based on the assumption that the target feature (in our case a crack) is not present in the image. Some simulations that we have performed suggest that, provided the feature covers only a small proportion of the image and does not have characteristics producing spikes in the spectrum (e.g., a straight line), the estimated spectrum is not very different from that obtained when the feature is absent. However, one can clearly envisage situations when the feature may be more extensive or has special characteristics. If these characteristics are known, this knowledge should be incorporated in the estimation procedure. If not, a more robust spectrum estimator may be required. There has been some research carried out on robust estimation of 1D spectra (e.g., [23]). However, these techniques are far more complicated than ours, and, in our view, would require considerable additional research to extend to two dimensions successfully.

APPENDIX A: DERIVATION OF $\hat{\text{Risk}}_1(p, q)$

The aim of this appendix is to show that the risk estimator $\hat{\text{Risk}}_1(p, q)$ defined by (6) is an unbiased estimator of $\text{Risk}_1(p, q)$. We begin by calculating $E(\text{RSS})$:

$$E(\text{RSS}) = E \sum_{s,t} (I_{st} - \hat{f}_{st})^2$$

$$= \sum_{s,t} E(I_{st}^2 - 2I_{st}\hat{f}_{st} + \hat{f}_{st}^2).$$

Since the ε_{st}'s are independent standard exponentials ($E(\varepsilon_{st}) = 1$ and $E(\varepsilon_{st}^2) = 2$), then $E(I_{st}) = f_{st}$, $E(I_{st}^2) = E(f_{st}^2\varepsilon_{st}^2) = 2f_{st}^2$, and

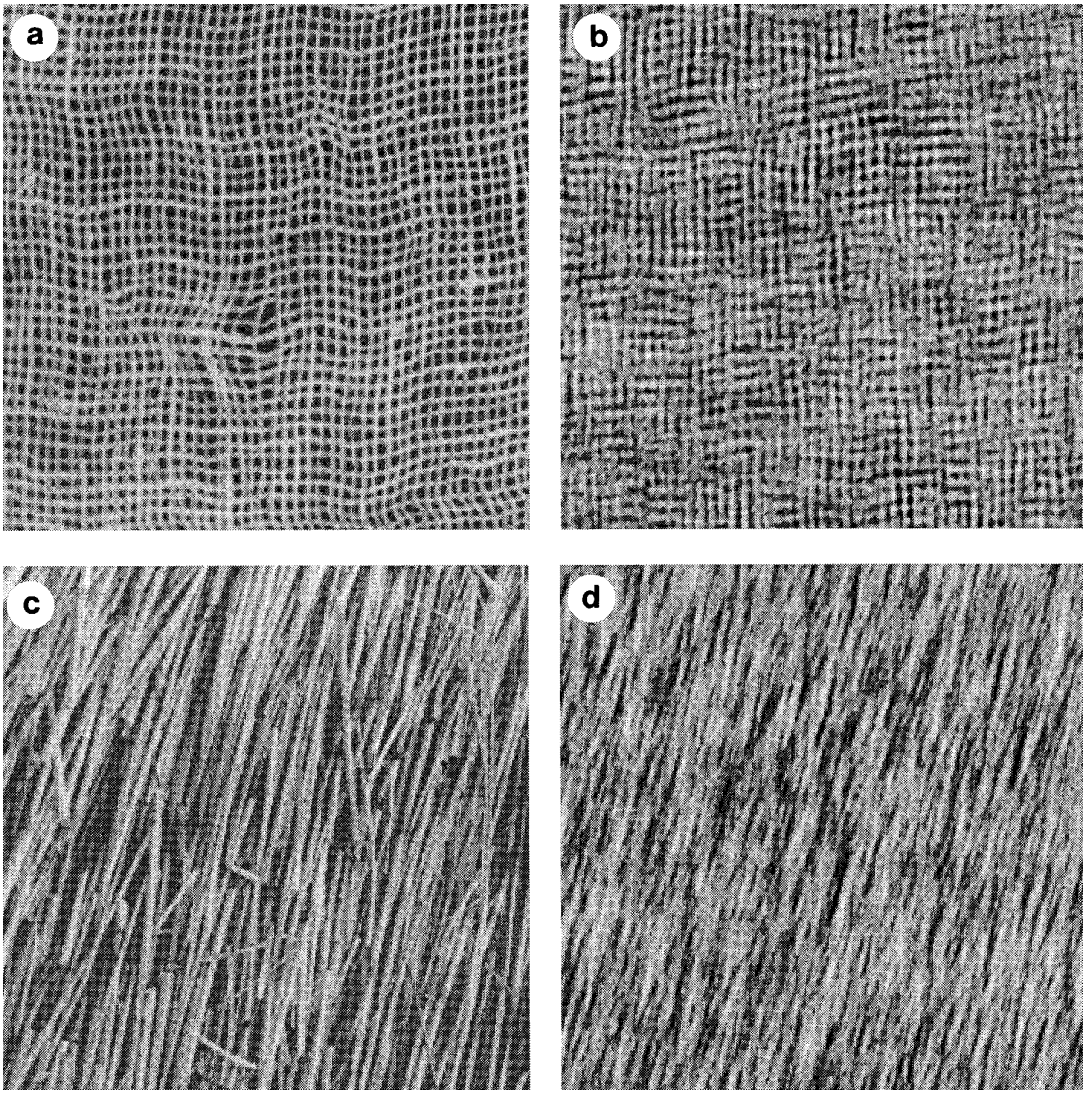

FIG. 9. Comparison of real and synthesized Brodatz's textures: results unsatisfactory. (a) real texture 3, (b) synthesized texture 3, (c) real texture 4, and (d) synthesized texture 4.

$$
\begin{aligned}
E(I_{st}\hat{f}_{st}) &= E\left(f_{st}\varepsilon_{st}\sum_{i=-p}^{p}\sum_{j=-q}^{q} w_{ij} f_{s+i,t+j}\varepsilon_{s+i,t+j}\right)\\
&= E\left(w_{00} f_{st}^2 \varepsilon_{st}^2 + \sum_{i\neq 0}\sum_{j\neq 0} w_{ij} f_{st}\varepsilon_{st} f_{s+i,t+j}\varepsilon_{s+i,t+j}\right)\\
&= 2w_{00} f_{st}^2 + \sum_{i\neq 0}\sum_{j\neq 0} w_{ij} f_{st} f_{s+i,t+j}\\
&= w_{00} f_{st}^2 + \sum_{i=-p}^{p}\sum_{j=-q}^{q} w_{ij} f_{st} f_{s+i,t+j}\\
&= w_{00} f_{st}^2 + f_{st}\sum_{i=-p}^{p}\sum_{j=-q}^{q} w_{ij} f_{s+i,t+j}\\
&= w_{00} f_{st}^2 + f_{st} E(\hat{f}_{st}).
\end{aligned}
$$

Therefore

$$
\begin{aligned}
E(I_{st} - \hat{f}_{st})^2 &= 2f_{st}^2 - 2(w_{00} f_{st}^2 + f_{st} E(\hat{f}_{st})) + E(\hat{f}_{st}^2)\\
&= E(f_{st} - \hat{f}_{st})^2 + (1 - 2w_{00}) f_{st}^2
\end{aligned}
$$

and

$$
E(\mathrm{RSS}) = n_1 n_2 \,\mathrm{Risk}_1(p,q) + (1 - 2w_{00}) E\left(\sum_{s,t}\frac{1}{2} I_{st}^2\right).
$$

Thus

$$
\hat{\mathrm{Risk}}_1(p,q) = \frac{\mathrm{RSS}}{n_1 n_2} - \frac{(1 - 2w_{00})}{2n_1 n_2}\sum_{s,t} I_{st}^2 \tag{10}
$$

is an unbiased estimator of $\mathrm{Risk}_1(p, q)$.

This idea of unbiased risk estimation has its origin in Mallows' C_p [22] and has been used by [30] and [7] to select the bandwidth for nonparametric curve estimation, by [38] and [12] to select the bandwidth for image restoration, and by [28] to select the bandwidth for emission computed tomography reconstruction. The crucial difference here is that in the present situation the variance of the noise (ε_{ij}) is known while in other situations the noise variance is usually unknown and has to be estimated.

APPENDIX B: SIMULATION OF SGRF

This appendix briefly describes how we have simulated an SGRF from a given spectrum f.

1. Let $\mathbf{f} = \{f_{st}\}$ denote the sampled version of f on the rectangular grid A, as defined in Section 2 (i.e., the image-representation of f), and let $\mathbf{g} = \{\sqrt{f_{st}}\}$.

2. Let $\boldsymbol{\delta}$ be a white noise image, of the same size as $\mathbf{f}$, with each of its pixels as a realization of the zero-mean unit-variance Gaussian distribution.

3. Compute the forward discrete Fourier transform of $\boldsymbol{\delta}$. Denote the corresponding real and imaginary parts by $\mathbf{u}$ and $\mathbf{v}$, respectively.

4. Compute $\mathbf{gu}$ and $\mathbf{gv}$, where the multiplication is pixelwise.

5. Compute the inverse discrete Fourier transform of the complex image ($\mathbf{gu}$, $\mathbf{gv}$). Then the real part of the resulting image is a realization of an SGRF generated from f.

Note that zero-padding can be applied to eliminate boundary effects when computing Fourier transforms.

ACKNOWLEDGMENTS

The authors thank Vic Solo, Mike Buckley, and Steve Marron for helpful discussions and Ed Breen for suggesting the stationarity transform (9). They also thank the referees for their comments.

REFERENCES

1. M. Berman, Automated smoothing of image and other regularly spaced data, *IEEE Trans. Pattern Anal. Mach. Intelligence* **16,** 1994, 460–468.
2. J. Besag, On the statistical analysis of dirty pictures, *J. Roy. Stat. Soc. Ser. B* **48,** 1986, 259–302.
3. D. R. Brillinger, *Time Series: Data Analysis and Theory,* expanded edition, Holden-Day, Oakland, CA, 1981.
4. P. Brodatz, *Textures: A Photographic Album for Artists & Designers.* Dover, New York, 1966.
5. M. J. Buckley, Fast computation of a discretized thin-plate smoothing spline for image data, *Biometrika* **81,** 1994, 247–258.
6. R. Chellappa and R. L. Kashyap, Texture synthesis using 2-D noncausal autoregressive models, *IEEE Trans. Acoustics Speech Signal Process.* **33,** 1985, 194–203.
7. S.-T. Chiu, Why bandwidth selectors tend to choose smaller bandwidths, and a remedy, *Biometrika* **77,** 1990, 222–226.
8. R. Dahlhaus and H. Kunsch, Edge effects and efficient parameter estimation for stationary random fields, *Biometrika* **74,** 1987, 877–882.
9. P. J. Diggle, *Statistical Analysis of Spatial Point Patterns,* Academic Press, San Diego, 1983.
10. D. E. Dudgeon and R. M. Mersereau, *Multidimensional Digital Signal Processing,* Prentice Hall, Englewood Cliffs, NJ, 1984.
11. J. Fan, T. Gasser, I. Gijbels, M. Brockmann, and J. Engel, *Local Polynomial Fitting: A Standard for Nonparametric Regression,* Discussion Paper 9315, Institute of Statistics, Catholic University of Louvain, Louvain-la-Neuve, 1993.
12. N. P. Galatsanos and A. K. Katsaggelos, Methods for choosing the regularization parameter and estimating the noise variance in image restoration and their relation, *IEEE Trans. Image Process.* **1,** 1992, 322–336.
13. S. Geman and D. Geman, Stochastic relaxation, Gibbs distributions, and the Bayesian restoration of images, *IEEE Trans. Pattern Anal. Mach. Intelligence,* **6,** 1984, 721–735.
14. C. M. Hurvich, Data-driven choice of a spectrum estimate: extending the applicability of cross-validation methods, *J. Am. Statist. Assoc.* **80,** 1985, 933–940.
15. A. K. Jain, *Fundamentals of Digital Image Processing,* Prentice Hall, Englewood Cliffs, NJ, 1989.
16. L. M. Kaplan and C.-C. J. Kuo, Texture roughness analysis and synthesis via Extended Self-Similar (ESS) model, *IEEE Trans. Pattern Anal. Mach. Intelligence* **17,** 1995, 1043–1056.
17. R. L. Kashyap, Characterization and estimation of two-dimensional ARMA models, *IEEE Trans. Inf. Theory* **30,** 1984, 736–745.
18. R. L. Kashyap and R. Chellappa, Estimation and choice of neighbours in spatial-interaction models of images, *IEEE Trans. Inf. Theory* **29,** 1983, 60–72.
19. S. W. Lang and J. H. McClellan, Multidimensional MEM spectral estimation, *IEEE Trans. Acoustics Speech Signal Process.* **30,** 1982, 880–886.
20. W. E. Larimore, Statistical inference on stationary random fields, *Proc. IEEE* **65,** 1977, 961–970.
21. T. C. M. Lee and M. Berman, Nonparametric estimation and simulation of two-dimensional Gaussian image textures, in *Proceedings of the Interface,* **28,** 1996, to appear.
22. C. L. Mallows, Some comments on C_p, *Technometrics* **15,** 1973, 661–675.
23. R. D. Martin and D. J. Thomson, Robust-resistant spectrum estimation, *Proc. IEEE* **70,** 1982, 1097–1115.
24. P. M. Narendra, A separable medium filter for image noise smoothing, *IEEE Trans. Pattern Anal. Mach. Intelligence* **3,** 1981, 20–29.
25. F. O'Sullivan, Discretized Laplacian smoothing by Fourier methods, *J. Am. Statist. Assoc.* **86,** 1991, 634–642.
26. R. Paget and D. Longstaff, Texture synthesis via a non-parametric Markov random field, in *Proceedings of DICTA 95, Digital Image Computing: Techniques and Applications,* pp. 547–552, 1995.
27. F. Palmer, *Adaptive Spectral Smoothing,* Technical Report ONR 30, Massachusetts Institute of Technology, Statistics Centre, 1983.
28. Y. Pawitan and F. O'Sullivan, Data dependent bandwidth selection for emission computed tomography reconstruction, *IEEE Trans. Med. Imag.* **12,** 1993, 167–172.
29. R. W. Picard, T. Kabir, and F. Liu, Real-time recognition with the entire Brodatz texture database, in *Proceedings of the IEEE Conference on Computer Vision and Pattern Recognition,* pp. 638–639, 1993.

30. J. A. Rice, Bandwidth choice for nonparametric regression, *Ann. Statist.* **12,** 1984, 1215–1230.
31. B. D. Ripley, *Spatial Statistics,* Wiley, New York, 1981.
32. B. Rosen and L. Vincent, Morphological image processing techniques applied to detection of correlogram tracks, *U.S. Navy J. Underwater Acoustics* **44,** 1994, 571–586.
33. A. Rosenfeld and A. Kak, *Digital Picture Processing,* second ed., Academic Press, San Diego, 1982.
34. G. Sharma and R. Chellappa, A model based approach for the estimation of 2-D maximum entropy power spectra, *IEEE Trans. Inf. Theory* **31,** 1985, 90–99.
35. G. Sharma and R. Chellappa, Two-dimensional spectrum estimation using noncausal autoregressive models, *IEEE Trans. Inf. Theory* **32,** 1986, 268–275.
36. B. Silverman, *Density Estimation for Statistics and Data Analysis,* Chapman & Hall, London, 1986.
37. V. Solo, Modeling of two-dimensional random fields by parametric cepstrum, *IEEE Trans. Inf. Theory* **IT-32,** 1986, 743–750.
38. V. Solo, Linear Image Restoration: An Analytical Study, Technical Report 88-VS-May-1988, Dept. of ECE, The Johns Hopkins Univ., Baltimore, MD, 1988.
39. J. K. Tugnait, Estimation of linear parametric models of nonGaussian discrete random fields with applications to texture synthesis, *IEEE Trans. Image Process.* **3,** 1994, 109–127.
40. M. P. Wand and M. C. Jones, Comparison of smoothing parameterizations in bivariate kernel density estimation, *J. Am. Statist. Assoc.* **88,** 1993, 520–528.
41. M. P. Wand and M. C. Jones, *Kernel Smoothing,* Chapman & Hall, London, 1995.
42. A. T. A. Wood and G. Chan, Simulation of stationary Gaussian process in $[0, 1]^d$, *J. Comput. Graphical Statist.* **3,** 1994, 409–432.